Supporting information

Nanodomains Coupled to Ferroelectric Domains Induced by Lattice Distortion in Self-Doped $LuMn_xO_{3\pm\delta}$ Hexagonal Ceramics

A. Baghizadeh,[a]* *Joaquim M. Vieira,*[a] *João N. Gonçalves,*[b] *Marc-Georg Willinger,*[c] *Marta C. Ferro,*[a] *Vitor S. Amaral,*[b]

[a]Department of Materials and Ceramic Engineering & CICECO, and [b] Physics Department & CICECO, Aveiro University, 3810-193 Aveiro, Portugal

[c]Department of Inorganic Chemistry, Fritz Haber Institute of the Max Planck Society, Faradayweg 4-6, Berlin, Germany

S.1. TEM sample preparation

Thin sections for the TEM study of $LuMn_xO_{3\pm\delta}$ ceramics were prepared by crushing and milling the pellets to fine powder, embedding the powders in microscopy resin which was sandwiched between two dummy slabs of single crystal silicon and finally cured. The mounting was mechanically polished down to 10 μm thickness or less judged by the transparency of silicon (red or yellow colors) and finished to electron transparency in several steps of ion milling using High Precision Dual Milling PIPS. In single mode

* Corresponding author:
Email address: ali.baghizhadeh@ua.pt (A.Baghizadeh)

ion milling, Ar ion energy is started from 5 keV (10 minutes), then is successively decreased to 4 keV (20 minutes), 3 keV until a minute hole appears inside silicon, continued with 2 keV and 1 keV for final etching, each with a hold of 10 minutes. The procedure ends with an additional ion milling step of 10 minutes at 1 keV in double mode ion milling. For all steps top and button ion guns were set at 4º to avoid serious ion beam damage on the edges of thinned particles.

S.2. Partial dislocations and twinning in basal plane view

Linked to magnetic measurements on current ceramics samples [1] and Figure 4 of the text of the manuscript, the nano-scale analysis of the basal plane distortion was done also for the sample x=0.92 of highest Mn vacancy nominal content. Figure S1.a gives the HRTEM image of a $LuMn_{0.92}O_{3\pm\delta}$ crystalline grain oriented along <001> zone axis where the trimmers of Mn ions can be seen. The simulated TEM image shown in the inset of this figure matches the TEM image. The bright spots are Lu ions in hexagonal symmetry and the gray spots inside the hexagons correspond to Mn trimmers of z = 0 and z = ½ planes. Figure S1.b gives the same model of the atomic structure for the <001> zone axis of the inset in Figure S1.a (O^{2-} ion not shown).

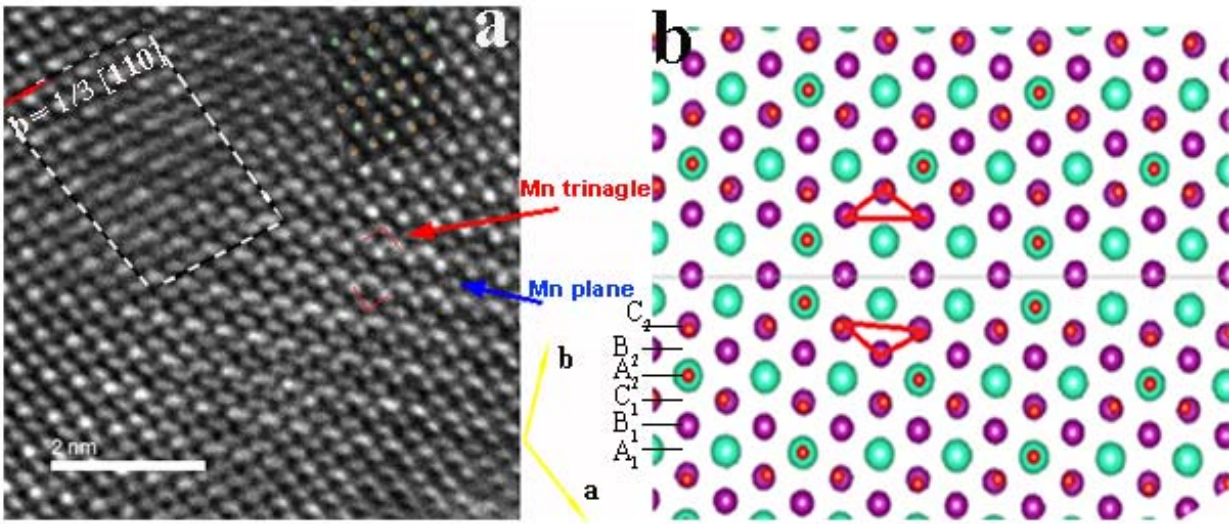

Figure S1. (a) <001> zone axis HRTEM image of sample $LuMn_{0.92}O_{3\pm\delta}$ with the planar defect made of a single plane of Mn ions between two planes of Lu ions (blue arrow). The inset shows the lattice simulation matching the TEM image. The dashed lines in (a) indicate the Burgers circuit in the area with a dislocation of Burgers vector 1/3[110] (red arrow). Two triangles (red) in the image point to twinning visible by following the discontinuity of the stacking sequence of ion layers on both sides of a single Mn plane marked (purple) in the image. The scale bar in the TEM image corresponds to 2 nm. (b) Model of twinning with a single plane of Mn ions as twin composition plane.

The single plane of Mn ions, the twinning plane in Figure S1.a and b, plays the role of mirror plane of the nano-twins. Two colored triangles are overlaid in Figure S1.a and b to single out the double-planes of Mn ions, showing the rotation by π of atomic layers around the <001> zone axis permitted by the symmetry of the lattice. As exhibited in Figure S1.b, the twinning corresponds to the modified sequence ion layers of $A_1B_1C_1A_2B_2C_2\mathit{A_1B_1A_1}C_2B_2A_2C_1B_1A_1$ instead of the regular sequence $A_1B_1C_1A_2B_2C_2$ … expected along [110] direction of the hexagonal basal plane. The distance between two adjacent Lu ions in hexagonal coordination is 5.6 Å, whereas distance between two Lu ions at both sides of the Mn mirror plane is just 3.9 Å. Shrinkage of the distance between two Lu ions can be explained as removal of one plane of the pair of Mn {110} planes leaving a single Mn plane in place, condensation of the excess of Mn vacancies being suggested. The same can be represented in the stacking sequence of atomic planes along the [T00] direction as the stacking fault created by the partial dislocation of Burgers vector **b** = -1/3[110]. The dashed arrow lines in Figure S1.a represent the Burgers circuit around the core of a partial dislocation with Burgers vector 1/3[110]. Shrinkage in the distance between two Lu layers is the result of the slip produced by the partial dislocation.

S.3. PDOS of selected $LuMn_xO_{3\pm\delta}$ compositions

To calculate the partial density of states (PDOS) of the concerned orbitals we used the full potential linearized augmented plane wave local orbital (APW+LO)[2] with generalized gradient approximation (PPB-GGA) for the exchange-correlation function [3] implemented in Wien2K 14.2. The magnetic ground state of $LuMnO_3$ is the AFM non-collinear configuration of Mn^{3+} ions in the basal plane [4]. A simpler magnetic configuration, already applied to $YMnO_3$ system [5], is used instead in the present work with the A-type AFM configuration with spins of Mn ions up in one plane and down in next plane, the total magnetic moment in a unit cell being zero. The choice for atomic spherical radii (in atomic units) was 2.15 for Lu, 1.67 for Mn and 1.48 for O ions. The number of plane waves in the interstitial regions was limited to $R_{MT}K_{max}$=7.0 as cut-off value. The electronic band gap is introduced in the structure by choosing U=6 eV in GGA+U to account for correlation effects[6] of the d-orbitals of the Mn ions. In both calculations, self-consistency was achieved on the 5×5×3 mesh containing 20 K-points in irreducible Brillouin zone (IBZ) with criteria of 0.00001 Ry and 0.0005 e for energy and charge, respectively. Figure S2 gives the calculated PDOS of relevant orbitals for $LuMn_xO_{3\pm\delta}$ samples with x=0.92 (a), x=1.00 (b) and x=1.08 (c).

Figures S2 show the PDOS for 5d, 2p and3d orbitals of oxygen, Lu and Mn. In the conduction band close to Fermi level, a large contribution comes from hybridization of Mn(3d) orbitals with O(2p) orbitals, mostly planar oxygen[5]. In contrast to the reported O K-edge measured by XAS in h-$RMnO_3$ materials [7-9], the energy resolution and statistics of EELS in the present study do not allow to distinguish different unoccupied states of the Mn(3d) orbitals in the pre-edge region of O K-edge separately. PDOS of Mn (3d) in Figures S2 implies that the first peak below 530 eV in Figure 5.a corresponds to mixing of unoccupied states of Mn-3d(3z2-r2)↑, (xz↓-yz↓) and (xy↓-x2-y2↓), and the second peak just above 530 eV shows Mn-3d(3z2-r2)↑ unoccupied states

with strong hybridization to O(2p) unoccupied states. The region above 533 eV in Figure 5.a displays Lu(5d)-O(2p) hybridized states, with two successive peaks of higher intensity than those peaks in the pre-edge region, revealing the nature of the strong bonding of Lu(5d)- O(2p) unoccupied states [10,11] claimed to be a probable driving force of ferroelectricity [8,10,12]. The stronger bonding featured by Lu(5d)-O(2p) for both planar and apical oxygen ions in Figure S2 for x=1.08 sample in comparison to the x=0 one represents the effect of chemically driven unit cell distortion on the Lu(5d)-O(2p) bond, which induces variation of intensity ratio in corresponding peaks of O K-edge in EELS spectra of Figure 5.a.

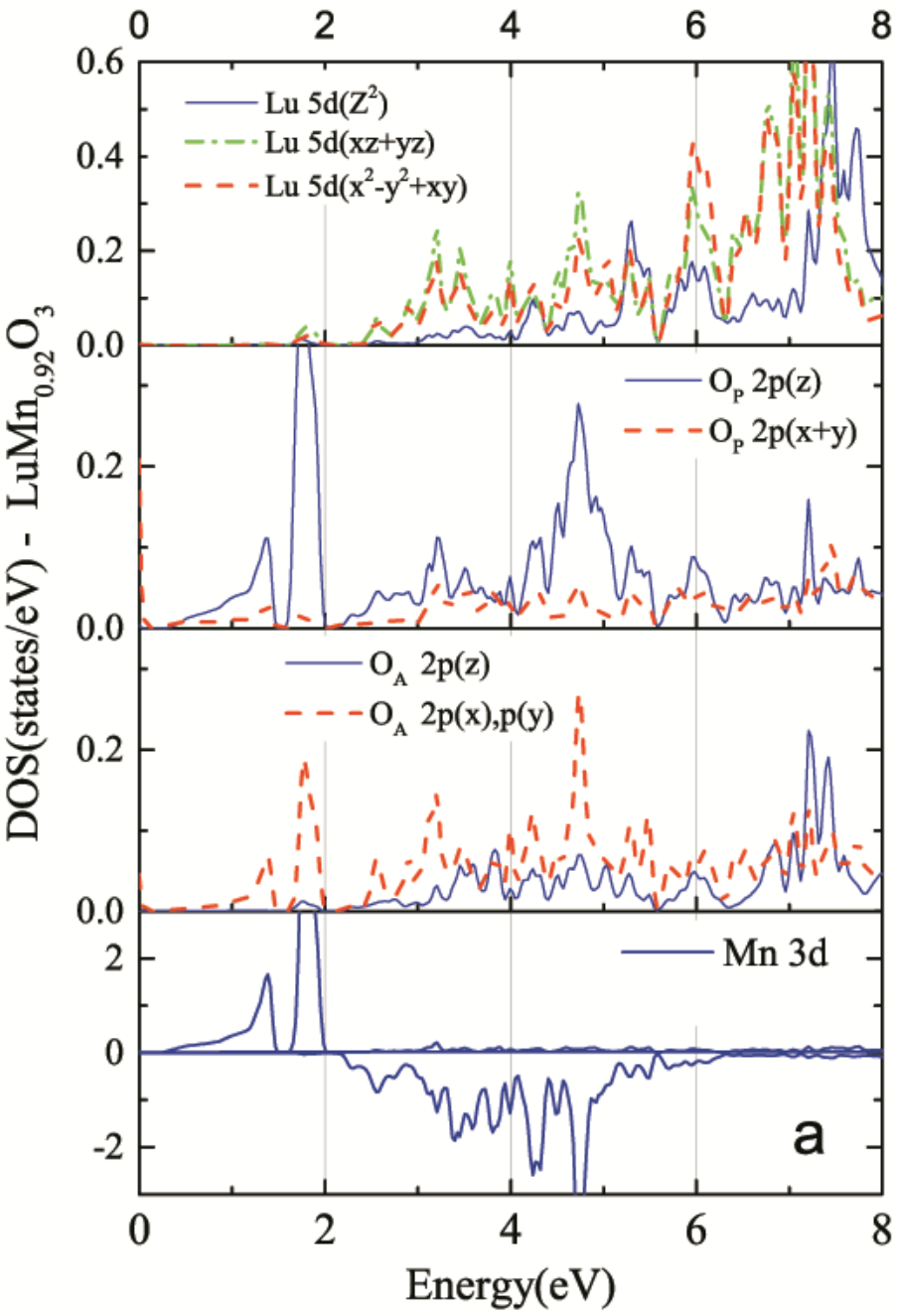
Lu 5d(Z²)
Lu 5d(xz+yz)
Lu 5d(x²-y²+xy)
O_P 2p(z)
O_P 2p(x+y)
O_A 2p(z)
O_A 2p(x),p(y)
Mn 3d
a
DOS(states/eV) - LuMn0.92O3
Energy(eV)

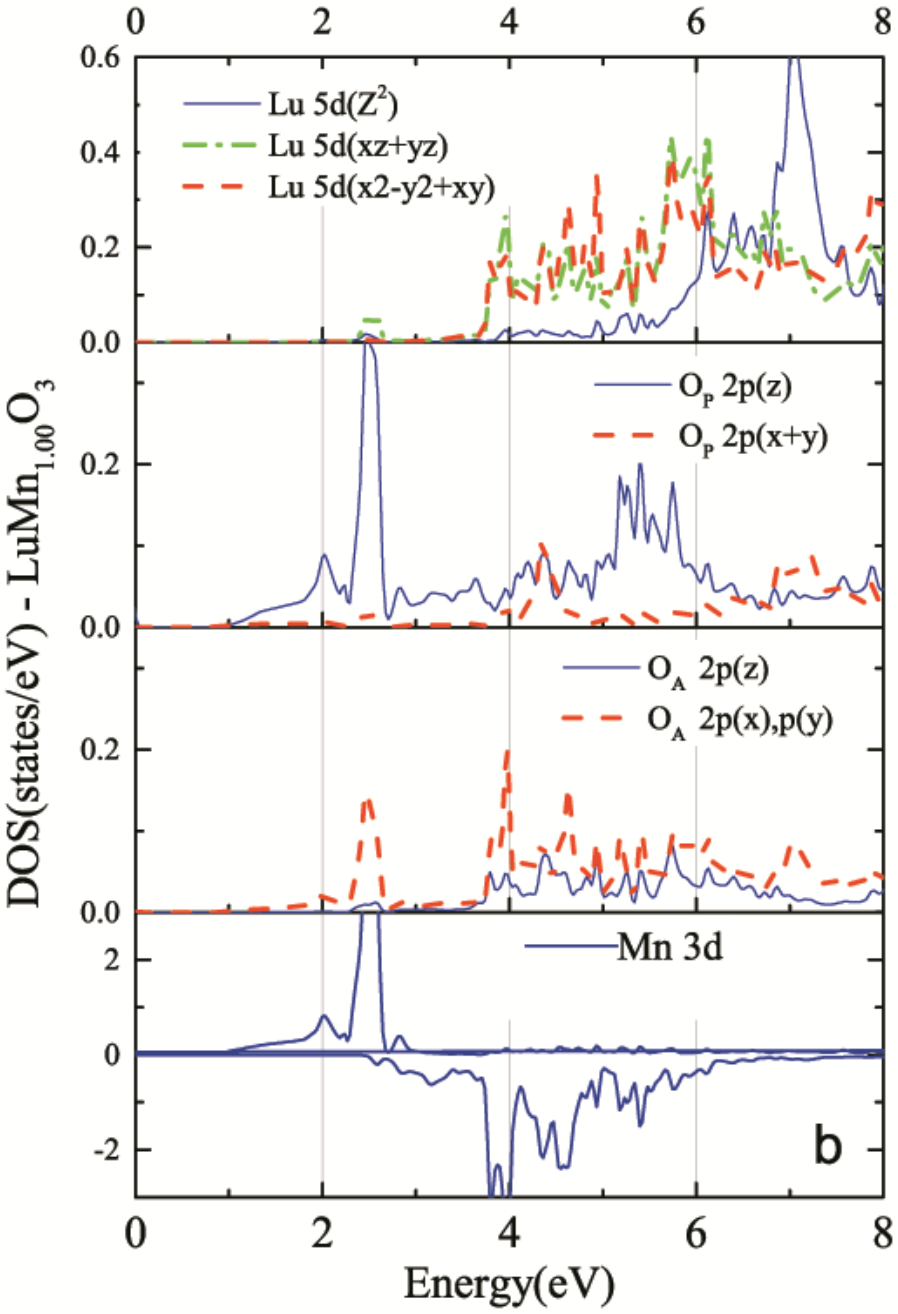
Lu 5d(Z²)
Lu 5d(xz+yz)
Lu 5d(x2-y2+xy)
O_P 2p(z)
O_P 2p(x+y)
O_A 2p(z)
O_A 2p(x),p(y)
Mn 3d
b
DOS(states/eV) - LuMn1.00O3
Energy(eV)

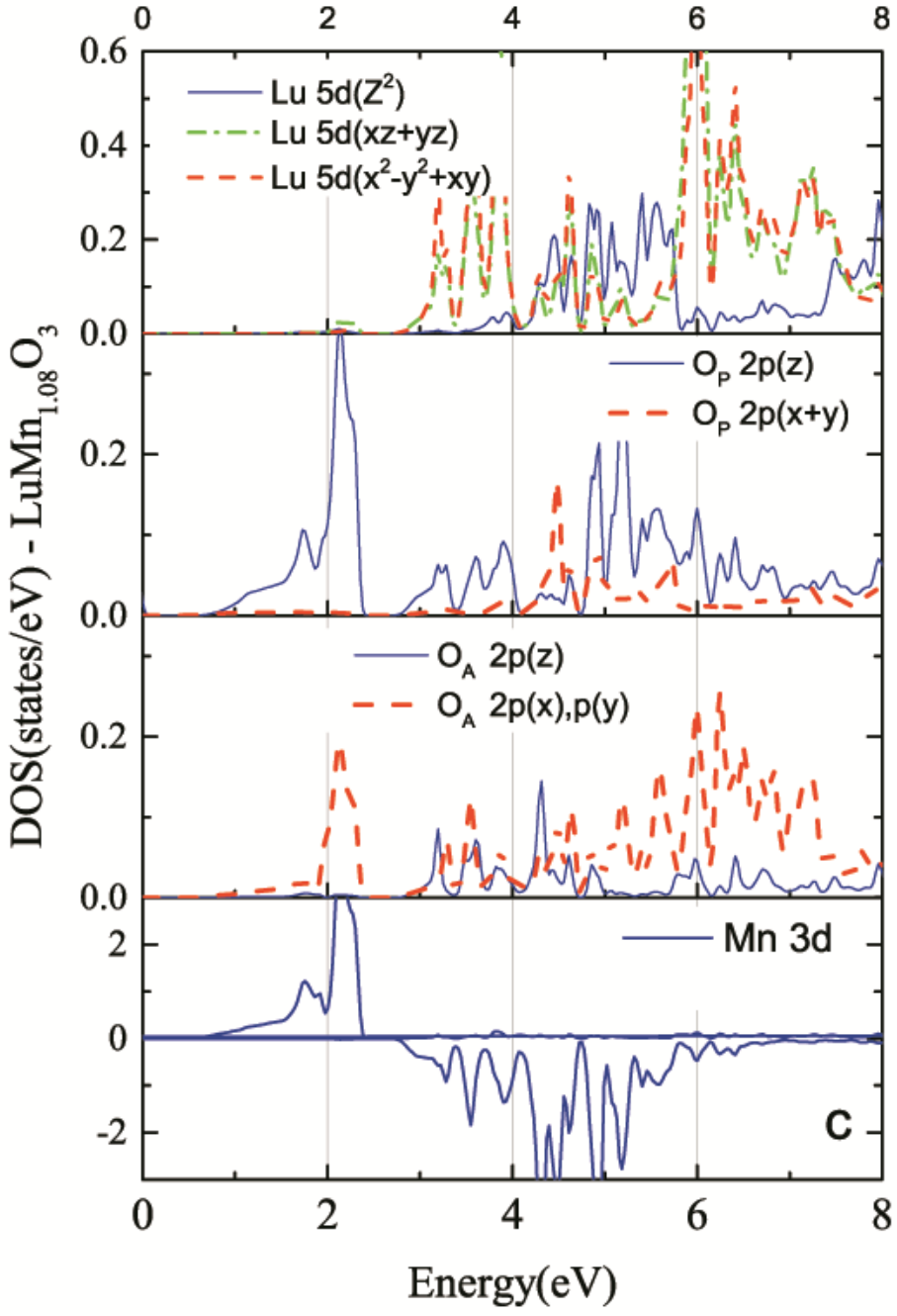

Figure S2. PDOS of the Lu(4d), O(2p) and Mn(3d) ions in (a) $LuMn_{0.92}O_{3\pm\delta}$, (b) $LuMn_{1.00}O_{3\pm\delta}$ and (c) $LuMn_{1.08}O_{3\pm\delta}$ bulk samples.

S.4. White-line ratio and oxidation state of Mn ions

EELS spectra of $L_{3,2}$ edges of Mn of the same samples of Figure 5.a are given in Figure S3.a. $L_{3,2}$ edges of transition metal ions have been extensively studied to provide useful information on oxidation state and coordination number of the transition metals [13,14]. L_3 and L_2 edges of Mn^{3+} ions result from electron transitions from $2p_{3/2}$ and $2p_{1/2}$ states to Mn 3d unoccupied states. The $L_{3,2}$ edges of Mn of three samples with different composition in Figure S3.a present similar shape and almost identical energy onset within the actual resolution of EELS. The intensity ratio of L_3/L_2 edges of Mn ion gives the Mn oxidation states, the so-called white-line ratio method being described elsewhere [15–18]. To apply the white-line ratio method to Mn $L_{3,2}$ edges of EELS spectra in Figure S3.a, the contribution of multiple scattering was subtracted using Digital Micrograph Suit. Then a 10 eV window was chosen as scaling window in the region immediately after L_2 peak to be used as Hartree-Slater cross section step function. The $L_{3,2}$ edges from the extracted step function were both integrated in the same energy window. The average L_3/L_2 ratio of two different particles of each composition is plotted in Figure S3.b. Based on known ranges of L_3/L_2 ratio corresponding to the Mn valence from literature [13–16,18], results in Figure S3.b point to constant Mn^{3+} oxidation state of the $LuMn_xO_{3\pm\delta}$ samples, or to a Mn valence state very close to 3+ by accounting that the nature of covalent bonding may result in slight changes in valence state of transition metal. Besides Mn valence state, $L_{3,2}$ edges were used to gauge crystal field environment of Mn ions because of their sensitivity to coordination number of Mn and therefore to Mn bonding to surrounding oxygen ions [13,19,20]. Compared to the h-$YMnO_3$ [13] the $L_{3,2}$ edges of off-stoichiometric samples in Figure S3.a closely match the one for x=1.00 sample and are in good agreement as well to the $L_{3,2}$ Mn edges of EELS in stoichiometric $YMnO_3$, all showing the same 3+ valence state for Mn ions.

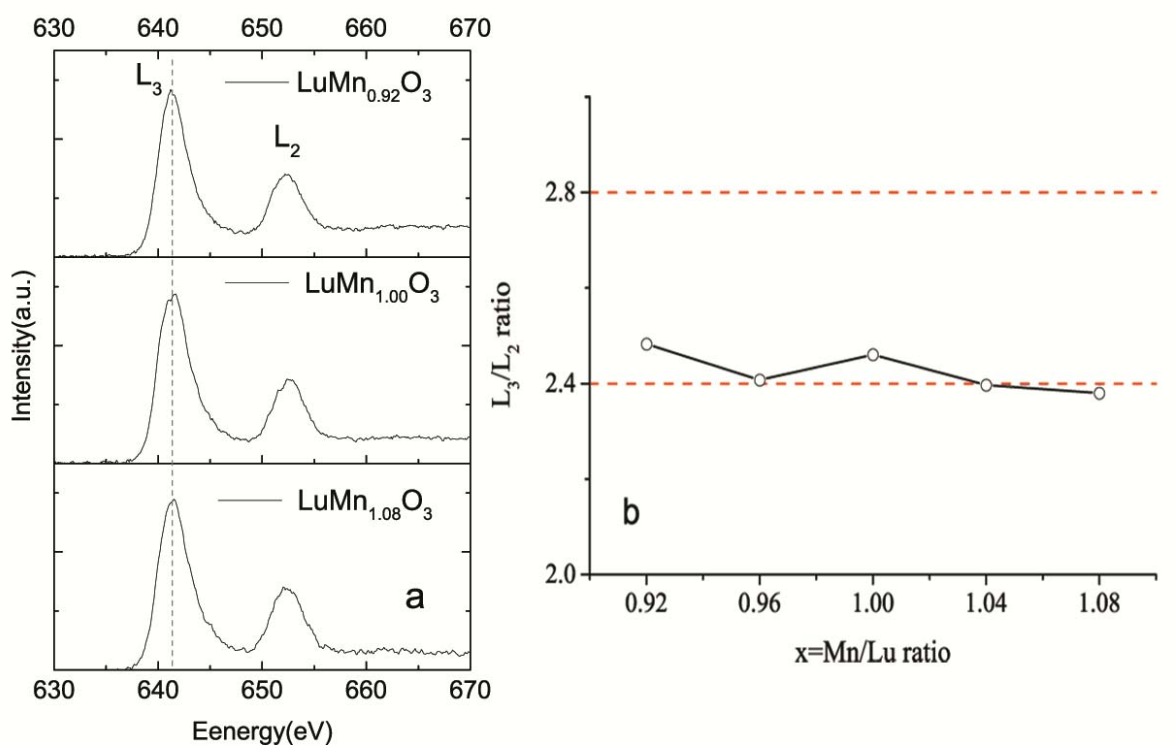

Figure S3. (a) EELS spectra of the Mn $L_{3,2}$ edges of the same three samples of Figure 5.a. showing a fixed energy onset, almost constant energy for the apex of L_3 peaks (dashed line in the (a)). (b) Values of L_3/L_2 white-line ratio for the $LuMn_xO_{3\pm\delta}$ samples of different composition, each value being the average of L_3/L_2white-line ratio of two different particles of the sample.

References:

(1) Baghizadeh, A.; Vieira, J. .; Amaral, J. S.; Graça, M. P.; Soares, M. R.; Mota, D. A.; Amaral, V. S. Crystal Structure, Magnetic and Dielectric Behavior of h-$LuMn_xO_{3\pm\delta}$ Ceramics ($0.95\leq x\leq 1.04$). J. Magn. Magn. Mater.2015, 395, 303–311.

(2) Blaha, P.; Schwarz, K.; Madsen, G. K. H.; Kvasnicka, K.; Luitz, J. An Augmented Plane Waves+Local Orbital Program for Calculating Crystal Properties. Karlheinz Schwarz, Techn. Universitat Wien, Austria 2001.

(3) Perdew, J. P.; Burke, K.; Ernzerhof, M. Generalized Gradient Approximation Made Simple. *Phys. Rev. Lett.* **1996**, *77* , 3865–3868.

(4) Fiebig, M.; Frohlich, D.; Kohn, K.; Leute, S.; Lottermoser, T.; Pavlov, V. V; Pisarev, R. V. Determination of the Magnetic Symmetry of Hexagonal Manganites by Second Harmonic Generation. *Phys. Rev. Lett.* **2000**, *84*, 5620–5623.

(5) Van Aken, B. B.; Palstra, T. T. M.; Filippetti, A.; Spaldin, N. a. The Origin of Ferroelectricity in Magnetoelectric $YMnO_3$. *Nat. Mater.* **2004**, *3*, 164–170.

(6) Medvedeva, J.E.; Anisimov, V.I.; Korotin, M.A.; Mryasov,O.N.; and Freeman, A.J. The Effect of Coulomb Correlation and Magnetic Ordering on the Electronic Structure of Two Hexagonal Phases of Ferroelectromagnetic $YMnO_3$. *J. Phys. Condens. Matter* **2000**, *12*, 4947.

(7) Kang, J.-S.; Han, S.; Park, J.-G.; Wi, S.; Lee, S.; Kim, G.; Song, H.; Shin, H.; Jo, W.; Min, B. Photoemission and X-Ray Absorption of the Electronic Structure of Multiferroic $RMnO_3$ (R=Y,Er). *Phys. Rev. B* **2005**, *71*, 092405.

(8) Cho, D.-Y. Y.; Kim, J.-Y. Y.; Park, B.-G. G.; Rho, K.-J. J.; Park, J.-H. H.; Noh, H.-J. J.; Kim, B. J. J.; Oh, S.-J. J.; Park, H.-M. M.; Ahn, J.-S. S.; et al. Ferroelectricity Driven by Y d0-Ness with Rehybridization in $YMnO_3$. *Phys. Rev. Lett.* **2007**, *98* , 217601.

(9) Liu, S.-H.; Huang, J.-C.-A.; Qi, X.; Lin, W.-J.; Siao, Y.-J.; Lin, C.-R.; Chen, J.-M. J. M. M.; Tang, M.-T.; Lee, Y.-H.; Lee, J.-C. J. M. M.; et al. Structural Transformation and Charge Transfer Induced Ferroelectricity and Magnetism in Annealed $YMnO_3$. *AIP Adv.* **2011**, *1*, 032173.

(10) Kim, J.; Cho, K. C.; Koo, Y. M.; Hong, K. P.; Shin, N. Y–O Hybridization in the Ferroelectric Transition of $YMnO_3$. *Appl. Phys. Lett.* **2009**, *95*, 132901.

(11) Asokan, K.; Jan, J. C.; Rao, K. V. R.; Chiou, J. W.; Tsai, H. M.; Mookerjee, S.; Pong, W. F.; Tsai, M.-H.; Kumar, R.; Husain, S.; et al. Electron- and Hole-Doping Effects on the Electronic Structure of Manganite Studied by X-Ray Absorption Spectroscopy. *J. Phys. Condens. Matter* **2004**, *16* , 3791–3799.

(12) Song, S.; Lee, J.-H.; Jang, H. M. Mode Coupling between Nonpolar and Polar Phonons

as the Origin of Improper Ferroelectricity in Hexagonal $LuMnO_3$. *J. Mater. Chem. C* **2014**, *2* , 4126.

(13) Nishida, S.; Kobayashi, S.; Kumamoto, A.; Ikeno, H.; Mizoguchi, T.; Tanaka, I.; Ikuhara, Y.; Yamamoto, T. Effect of Local Coordination of Mn on Mn-$L_{2,3}$ Edge Electron Energy Loss Spectrum. *J. Appl. Phys.* **2013**, *114*, 054906.

(14) Tan, H.; Verbeeck, J.; Abakumov, A.; Van Tendeloo, G. Oxidation State and Chemical Shift Investigation in Transition Metal Oxides by EELS. *Ultramicroscopy* **2012**, *116*, 24–33.

(15) Varela, M.; Oxley, M. P.; Luo, W.; Tao, J.; Watanabe, M.; Lupini, A. R.; Pantelides, S. T.; Pennycook, S. J. Atomic-Resolution Imaging of Oxidation States in Manganites. *Phys. Rev. B* **2009**, *79*, 085117.

(16) Schmid, H. K.; Mader, W. Oxidation States of Mn and Fe in Various Compound Oxide Systems. *Micron* **2006**, *37*, 426–432.

(17) Pearson, D.; Ahn, C.; Fultz, B. White Lines and D-Electron Occupancies for the 3d and 4d Transition Metals. *Phys. Rev. B* **1993**, *47*, 8471–8478.

(18) Riedl, T.; Gemming, T.; Wetzig, K. Extraction of EELS White-Line Intensities of Manganese Compounds: Methods, Accuracy, and Valence Sensitivity. *Ultramicroscop* **2006**, *106* , 284–291.

(19) Garvie, L. A. J.; Craven, A. J. High-Resolution Parallel Electron Energy-Loss Spectroscopy of Mn $L_{2,3}$-Edges in Inorganic Manganese Compounds. *Phys. Chem. Miner.* **1994**, *21*,191-206.

(20) Wu, K. H.; Gou, I. C.; Luo, C. W.; Uen, T. M.; Lin, J.-Y.; Juang, J. Y.; Kobayashi, T.; Chen, C. K.; Lee, J. M.; Chen, J. M. Polarization-Dependent X-Ray Absorption Spectroscopy of Hexagonal and Orthorhombic $TbMnO_3$ Thin Films. *J. Phys. Conf. Ser.* **2010**, *200* , 012227.